nature nanotechnology

REVIEW ARTICLE

https://doi.org/10.1038/s41565-021-01068-y

Excitons in semiconductor moiré superlattices

Di Huang[1]✉, Junho Choi[1,2], Chih-Kang Shih[1,2] and Xiaoqin Li[1,2]✉

Semiconductor moiré superlattices represent a rapidly developing area of engineered photonic materials and a new platform to explore correlated electron states and quantum simulation. In this Review, we briefly introduce early experiments that identified new exciton resonances in transition metal dichalcogenide heterobilayers and discuss several topics including two types of transition metal dichalcogenide moiré superlattice, new optical selection rules, early evidence of moiré excitons, and how the resonant energy, dynamics and diffusion properties of moiré excitons can be controlled via the twist angle. To interpret optical spectra, it is important to measure the energy modulation within a moiré supercell. In this context, we describe a few scanning tunnelling microscopy experiments that measure the moiré potential landscape directly. Finally, we review a few recent experiments that applied excitonic optical spectroscopy to probe correlated electron phenomena in transition metal dichalcogenide moiré superlattices.

When two atomically thin van der Waals (vdW) layers are vertically stacked together, the atomic alignment between the layers exhibits periodic variations, leading to a new type of in-plane superlattice known as the moiré superlattice (MSL). The period of MSLs is determined by the lattice constant mismatch and the twist angle between the two layers. Two types of MSL are most widely studied: those formed via twisted graphene layers and those formed via twisted transition metal dichalcogenide (TMD) layers.

The most striking properties of twisted bilayer graphene emerge from the flat bands at the so-called magic angles[1]. Correlated insulator states and unconventional superconductivity have been observed near the first magic angle of 1.1° within a narrow range of 0.1° (refs. [2–6]). Flat bands are found in other twisted two-dimensional (2D) materials, including TMDs, leading to strongly correlated electronic phases[7–12]. However, the nature of the flat bands in TMDs and graphene bilayers is very different. The variation of the interlayer spacing in TMD MSLs is larger than that found in graphene MSLs, leading to variation of the interlayer hybridization within a supercell and the formation of flat bands in TMD MSLs[13]. Compared with graphene, TMD MSLs possess several advantages. First, the existence of a sizeable bandgap leads to thermal stability, light emission and robust switching behaviour. Second, large spin–orbit coupling provides rich opportunities for engineering of topological bands and optical control of spins/valleys. Last, the flat bands in TMD bilayers exist over a wide range of twist angles instead of at discrete magic angles, making them comparatively easy to realize experimentally[7,13,14].

TMD MSLs are semiconductors with a sizeable bandgap, and their optical properties are dominated by bound electron–hole pairs known as moiré excitons. Similar to excitons in TMD monolayers[15–17], the reduced Coulomb screening in atomically thin layers leads to a large binding energy, making these quasiparticles stable at room temperature and relevant for various optoelectronic devices. We focus on the fundamental properties of these important optical excitations and hope to provide updated references in this rapidly evolving field[18–20].

The Review is organized into several sections. We first discuss the various species of excitons found in TMD bilayers. We then explain how the moiré potential imposes new optical selection rules and review scanning tunnelling microscopy (STM) experiments that have quantified the moiré potential and localized electronic states. After that, we review early experiments that identified the optical spectroscopy signatures of moiré excitons. It has been realized more recently how moiré exciton dynamics and diffusion can be controlled via the twist angle. Finally, we introduce the recent progress reported on twisted TMD bilayers acting as a robust platform to realize correlated electron states at a higher temperature than those in magic-angle twisted bilayer graphene. These correlated states can be probed via the optical spectroscopy of moiré excitons.

New exciton resonances and selection rules

New exciton resonances emerge in TMD bilayers even in the absence of a clearly defined moiré potential[19,21,22]. In a simple picture, if the electron and hole primarily reside in different (the same) monolayers, they are referred to as interlayer (intralayer) excitons, as illustrated in Fig. 1a. Furthermore, there are situations where the electron (e) (or hole (h)) wavefunction is distributed over both layers, and these excitons are referred to as hybrid excitons (Fig. 1b). In most cases, the TMD heterostructures have a type II band alignment[23–26], leading to a rapid charge/energy transfer[27–30] and the formation of long-lived interlayer excitons at lower energies than for the intralayer excitons[21,22,31–33].

Because the interlayer excitons are spatially indirect, their dipole moment is greatly reduced compared with that of intralayer excitons, that is, by approximately one or two orders of magnitude[34–37]. As a result, intralayer excitons dominate the optical absorption spectra. Both interlayer and intralayer excitons may appear in photoluminescence (PL) spectra. Some have argued that the stronger interlayer exciton PL than that of intralayer excitons indicates clean and high-quality interfaces[22,27,38]. Hybrid excitons appear in TMD heterostructures when the conduction bands or the valence bands between the two layers are close in energy[24–26,39]. For example, hybrid excitons have been observed in $MoSe_2/WS_2$ (WSe_2/WS_2) heterostructures where the electrons (holes) are distributed in both layers, and such wavefunction distribution can be controlled using an electric field applied perpendicular to the 2D plane[40–42]. Such hybridization is also very strong in twisted homobilayers[43]. Few optical experiments have been performed on twisted TMD homobilayers[44,45]. Their properties can be more complex due to both hybridization and possible lattice reconstruction over a rather large

[1]Physics Department and Center for Complex Quantum Systems, The University of Texas-Austin, Austin, TX, USA. [2]Texas Materials Institute and Center for Dynamics and Control of Materials, The University of Texas-Austin, Austin, TX, USA. ✉e-mail: idgnauh@utexas.edu; elaineli@physics.utexas.edu

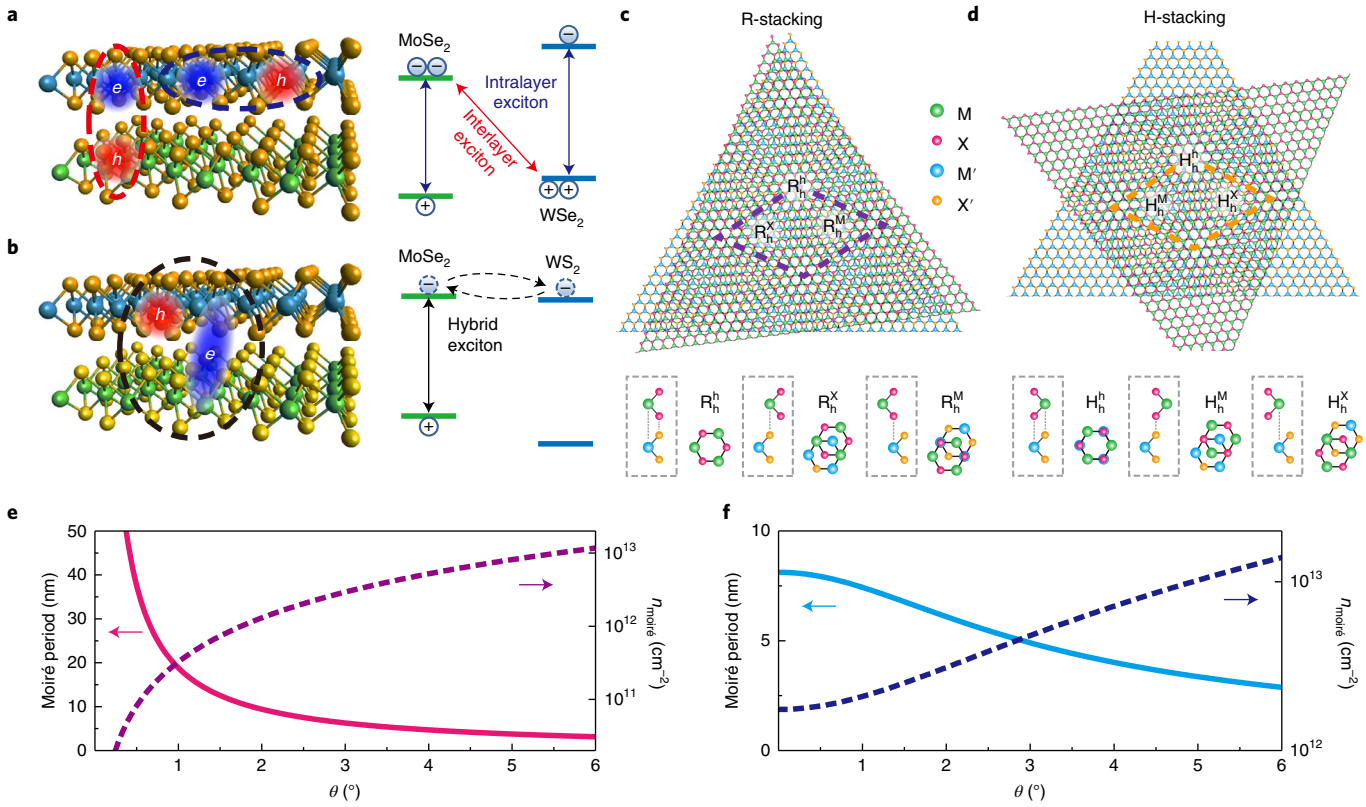

Fig. 1 | Excitons and MSLs in TMD heterobilayers. a,**b**, Illustration of the spatial distribution and energy diagrams of intralayer and interlayer excitons (**a**) and hybrid excitons (**b**). **c**,**d**, Near-R-stacked (**c**) and near-H-stacked (**d**) MSLs. In both **c** and **d**, the heterostructure consists of the electron-layer MX_2 and hole-layer $M'X'_2$, with the M, X, M′ and X′ atoms in green, magenta, blue and gold colours, respectively. The purple and orange dashed diamond shapes indicate one supercell of the R- and H-stacking MSL. **e**,**f**, The moiré period and density of the moiré supercells (the number of moiré supercells per square centimetre) as a function of the twist angle in near-commensurate MSL (**e**; for example, $MoSe_2/WSe_2$) and in incommensurate MSL (**f**; for example, $WS_2/MoSe_2$) with near-*R*-stacking. Solid (dashed) lines indicate the moiré period (moiré supercell density). θ is the twist angle between the top and bottom layers in the heterostructure.

range of twist angles[45–49]. In view of these challenges we omit the discussion of twisted homobilayers in most sections of this Review.

TMD heterostructures close to commensurate stacking can be categorized by two stacking orders: near-rhombohedral stacking (R-stacking) or near-hexagonal stacking (H-stacking). In both stacking orders, one can identify several high-symmetry points as depicted in Fig. 1c,d. In this Review, we use the notation $R(H)^{h/X/M}_h$ to represent these local electronic states, where R/H indicates the stacking order, and the superscript indicates the hexagonal lattice centre (h), chalcogen atom (X) or metal atom (M) in the electron layer, which is aligned to the hexagonal centre (h) in the hole layer as represented by the subscript[19,50]. In the literature reviewed, a variety of notations have been used. We summarize some examples in Table 1 to help clarify these notation types. Different interlayer atomic registries lead to a modulation of the energy landscape, interlayer spacing and atomic reconstruction in MSLs[50–54].

It is also helpful to distinguish between the two types of heterostructure: near-commensurate and incommensurate heterostructures, depending on whether the two layers share the same chalcogen atoms. In near-commensurate heterostructures consisting of two TMD monolayers that share the same chalcogen atoms, the lattice constants are very similar, leading to a large range of possible moiré supercell sizes (~1–100 nm) or supercell densities ($n_{moiré}$), as shown in Fig. 1e[24,55,56]. In near-commensurate heterostructures (for example, $MoSe_2/WSe_2$) grown using chemical vapour deposition (CVD), the crystalline axes tend to align to minimize the energy. The lattice in each layer deforms slightly and a completely commensurate structure can form, that is, no moiré patterns exist[49,57]. By contrast, in incommensurate heterostructures consisting of two TMD monolayers with different chalcogen atoms (for example, MoS_2/WSe_2), the lattice constants differ substantially (by ~4%). The largest possible moiré supercell is ~8 nm laterally (Fig. 1f)[58–60]. Therefore, the tunable range of the supercell size and density is reduced in incommensurate heterostructures compared with those in near-commensurate heterostructures. This difference can lead to different twist-angle-dependent optical properties.

Table 1 | Notation examples for high-symmetry locations in different literature reports

No.	R-stacking			H-stacking			Ref.
1	R^h_h	R^X_h	R^M_h	H^h_h	H^X_h	H^M_h	19,50
2	$R^{M'/M}$	$R^{X'/M}$	$R^{M'/X}$	$H^{X'/M}$	$H^{M'/M}$	$H^{X'/X}$	71
3	AA	$AB_{M'}$	$AB_{X'}$	N/A	N/A	N/A	54,78
4	AA	$B^{M/X'}$	$B^{X/M'}$	AB	$B^{M/M'}$	$B^{X/X'}$	51,69,80
5	AA	AB	BA	AA′	A′B	AB′	13
6	$R^X_{X'}$ or $R^M_{M'}$	$R^M_{X'}$	$R^X_{M'}$	$H^X_{M'}$ or $H^M_{X'}$	$H^M_{M'}$	$H^X_{X'}$	53

The heterostructure in this table is assumed to be made up of electron-layer material MX_2 and hole-layer material $M'X'_2$. Notation numbers 1 and 3 use the atom on the hexagon centre in another layer to denote the bilayers, whereas numbers 2, 4 and 6 denote the bilayers by means of the well-aligned atoms in both layers.

Box 1

In one moiré supercell of an R-stacked MSL, there are three high-symmetry points (R_h^h, R_h^X and R_h^M) where the local atomic registry preserves the three-fold rotational symmetry $\hat{C}_3$. The optical selection rule is not only determined by the atomic magnetic quantum numbers but also by the Bloch phase factor under $\hat{C}_3$ operations. The Bloch phase shift is different at each of the three high-symmetry points[50,70]. Here, we discuss the optical transitions at the K valley. The interlayer exciton wave packet and photons must share the same rotational symmetry. As a result, the exciton wave packet at R_h^h (R_h^X) couples to σ^+ (σ^-) light only, whereas the dipole at R_h^M is perpendicular to the 2D plane, thus it does not couple to incident plane waves effectively as illustrated in **a**[50,52,74]. These high-symmetry points are also the energy extrema of the moiré potential. Photoexcited carriers could form excitons at these different sites if the barriers between neighbouring local energy minima are reasonably high. In this picture, the MSL potential imposes a spatial modulation of the optical selection rules (shown in **b**). Selection rules in H-stacked MSLs are also analysed in detail in ref. [74].

Even at a single location within the moiré supercell, one may expect multiple exciton resonances[50,52,139]. Because of the large energy modulation (~100–300 meV depending on the material combinations and stacking orders) introduced by the moiré potential, one may expect to observe both ground-state and excited-state excitons (shown in **c**). These states also obey alternating optical selection rules, as suggested by the theoretical calculations shown in **d**. Ground and excited exciton states are routinely observed in InAs self-assembled quantum dots[50,52,104].

Thus, two possible microscopic pictures lead to multiple interlayer exciton resonances with alternating selection rules. Current experiments cannot be used to validate or rule out one of these two pictures definitively. We also caution that PL is not the optimal experimental technique for determining the optical selection rules because PL involves a multi-step relaxation process. Instead, absorption-type techniques (either linear absorption or pump/probe methods) are preferred[140]. Because of the small dipole moments associated with the interlayer excitons, however, absorption measurements on interlayer excitons can be quite challenging. These microscopic pictures are also simplified descriptions of the exciton distributions. In real materials, the electron and hole wavefunction may be distributed in different sites within a moiré supercell.

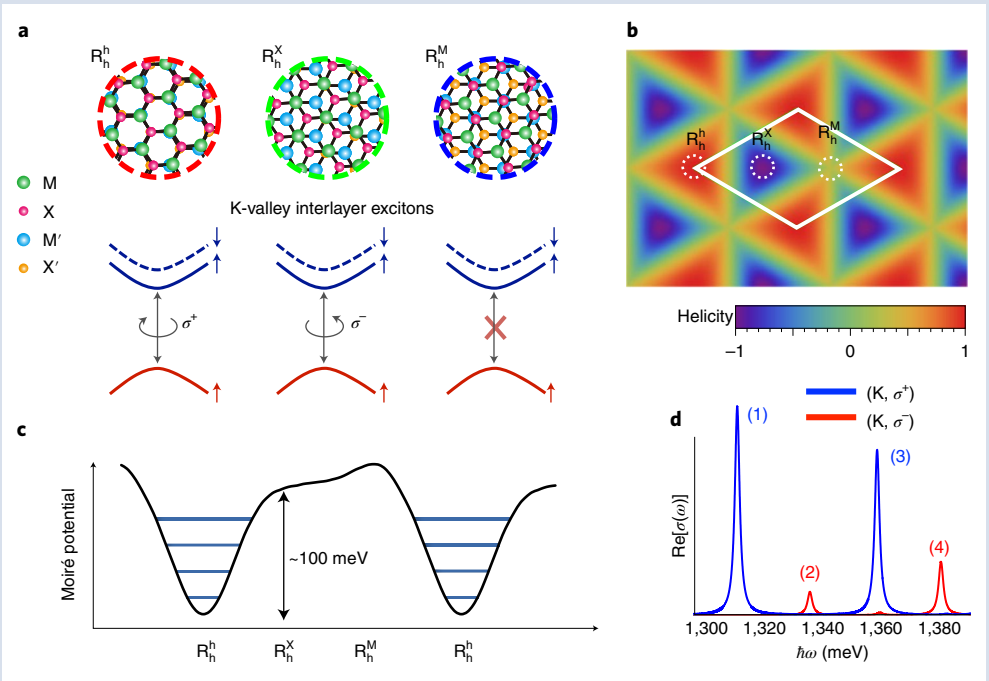

Interlayer exciton optical selection rules in MSLs. a, Local atomic alignments of three high-symmetry points (the white dashed circles in **b**) and their corresponding interlayer exciton selection rules in the K valley. **b**, Spatial modulation of optical selection rules for excitons localized at different locations of the supercell. The supercell of the MSL is highlighted by the white diamond shape. **c**, Illustration of multiple interlayer exciton states confined at a global minima within the moiré supercell. **d**, Calculated absorption spectrum for the ground and excited states exhibiting alternating selection rules. Panels **a**–**d** adapted with permission from ref. [82], Springer Nature Ltd.

Early optical experiments on TMD heterostructures have identified different types of exciton[19,27,31,41,61–64] and investigated ultrafast charge transfer[27,28,65], polarization-dependent dynamics[32,64,66,67] and valley-polarized diffusion[68]. These early experiments were often performed on heterostructures without hexagonal boron nitride (hBN) encapsulation and, thus, the moiré pattern is probably highly disordered. In addition, early experiments do not report accurate information on the twist angle, which is critical in controlling the electronic bands and exciton properties. Thus, it is difficult to identify the influence of the moiré potential in these early experiments.

In the presence of MSLs, the original Brillouin zones of individual layers are reduced to the moiré Brillouin zone (MBZ), introducing

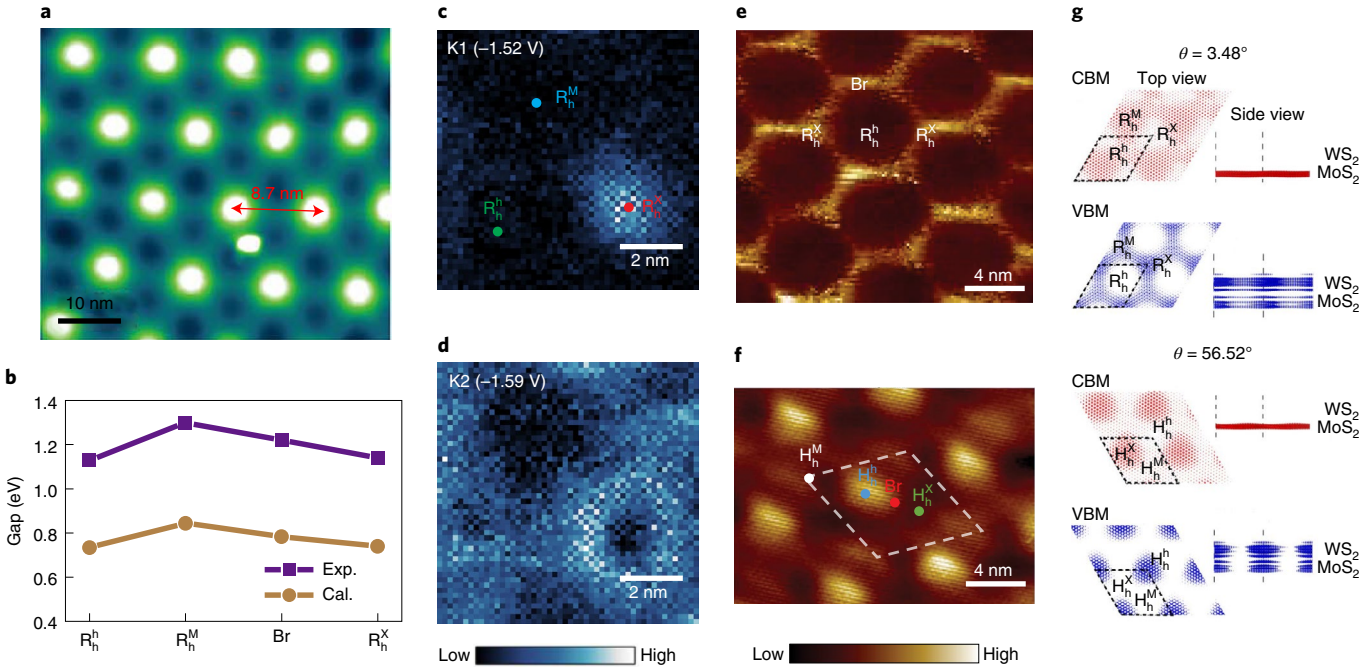

Fig. 2 | Unveiling the moiré local bandgap and flat bands via STM/S. a, MSL formed in a CVD-grown MoS_2/WSe_2 bilayer with aligned crystalline axes. **b**, Energy gap measured (Exp.) and theoretically calculated (Cal.) at different high-symmetry points. Br refers to bridge point between two high symmetry points. **c**,**d**, In an R-stacked WSe_2/WS_2 bilayer with near-zero twist angle, d*I*/d*V* mapping showing the localized moiré flat bands originating from the valence bands near the K points probed using different tip bias voltages of −1.52 V (**c**) and −1.59 V (**d**). The dots in panel **c** stand for R_h^h (green), R_h^X (red) and R_h^M (blue). **e**,**f**, The d*I*/d*V* mapping showing the topmost valence band near the K points as localized moiré flat bands in 3° (**e**) and 57.5° (**f**) twisted WSe_2 homobilayers. **g**, First-principles calculations showing the top and side views of the charge density of the CBM and VBM states for MoS_2/WS_2 heterostructures with twist angles (θ) of 3.48° (top panel) and 56.52° (bottom panel). CBM, conduction band minimum; VBM, valence band maximum. The supercell of the MSL is highlighted by the dashed diamond shapes in **f** and **g**. Panels adapted with permission from: **a**,**b**, ref. [54], AAAS under a Creative Commons license CC BY 4.0; **c**,**d**, ref. [51], Springer Nature Ltd; **e**,**f**, ref. [80], Springer Nature Ltd; **g**, ref. [71], AAAS under a Creative Commons license CC BY 4.0.

folded bands[13,50,52,69–71]. Furthermore, the moiré potential modulation mixes momentum states separated by the moiré reciprocal lattices and lifts the degeneracy between the exciton states at the MBZ corners. The moiré exciton dispersion can be measured from the evolution of multiple exciton resonances as a function of the twist angle[52,72]. For a given MSL, multiple intralayer and interlayer exciton resonances are predicted. We explain the optical selection rules expected for interlayer excitons at the K valley in TMD heterobilayers with an R-stacked MSL in Box 1. The selection rules are different for H-stacked bilayers where triplet states are also bright[70,73,74], as theoretically predicted and experimentally observed[75]. In TMD monolayers, circularly polarized light can be used to access a particular valley because of the spin-valley-locked selection rules for excitons at the K and K′ valleys. In TMD MSLs, however, different exciton resonances at a given valley can absorb light with different circular polarizations. Although an exciton resonance can still be associated with a particular valley, photon helicity is no longer locked to a particular valley[70]. Thus, accessing and manipulating the valley index via moiré excitons are more challenging.

Measurement of moiré potential

Experimental measurements of the moiré potential together with first-principles calculations of band structures are the foundations for interpreting optical experiments. Most calculations only compute the local electronic bands at a few selected high-symmetry points and extrapolate for other locations within the supercells. The conventional method of computing excitons in semiconductors, GW–Bethe–Salpeter equation, is too expensive to apply in the case of moiré excitons because of the large number of atoms included in a moiré supercell[76]. Alternative approaches, such as those based on time-dependent density functional theory, have been recently developed to address this challenge[71].

Given its high spatial and energy resolution for electronic states, scanning tunnelling microscopy and spectroscopy (STM/S) is an ideal technique to probe the local electronic states in MSLs. Zhang et al. mapped the MSL and its potential in a CVD-grown rotationally aligned R-stacked MoS_2/WSe_2 bilayer, as illustrated in Fig. 2a[54]. The local band gaps at different high-symmetry points within the moiré supercell were found to vary by ~200 meV at ~77 K with minimal gaps found at the R_h^h or R_h^X points, as shown in Fig. 2b. Another experiment on the H-stacked $MoSe_2/WSe_2$ bilayer reported an even deeper energy landscape for the valence (~300 meV) and conduction bands (~150 meV) at the H_h^h site[53]. The spatial distribution of these local electronic states was further visualized using STS mapping. However, this STM/S measurement[53] did not offer any resolution in momentum space. Therefore, the moiré potential depth cannot be directly related to excitons at the K or Q valleys.

On an R-stacked MoS_2/WSe_2 bilayer, Feenstra and collaborators revealed that the flat bands at both the K point in the conduction band and the Γ point in the valence band are localized by the moiré potentials at 4 K (refs. [77,78]). They further confirmed that such localized states are absent in a bilayer with a twist angle of approximately 15°. Two flat valence bands at the *K* point were identified at the R_h^X site in WSe_2/WS_2 bilayer by Li et al., as illustrated in Fig. 2c,d[51]. The formation of these localized states with an energy spacing of tens of millielectronvolts is consistent with the predicted flat bands in TMD MSLs[13,50,52,71,79].

The localized flat bands in R-stacked and H-stacked WSe_2 twisted bilayers differ notably, as explicitly measured in Fig. 2e,f[80]. These different spatial distributions of conduction band minimum

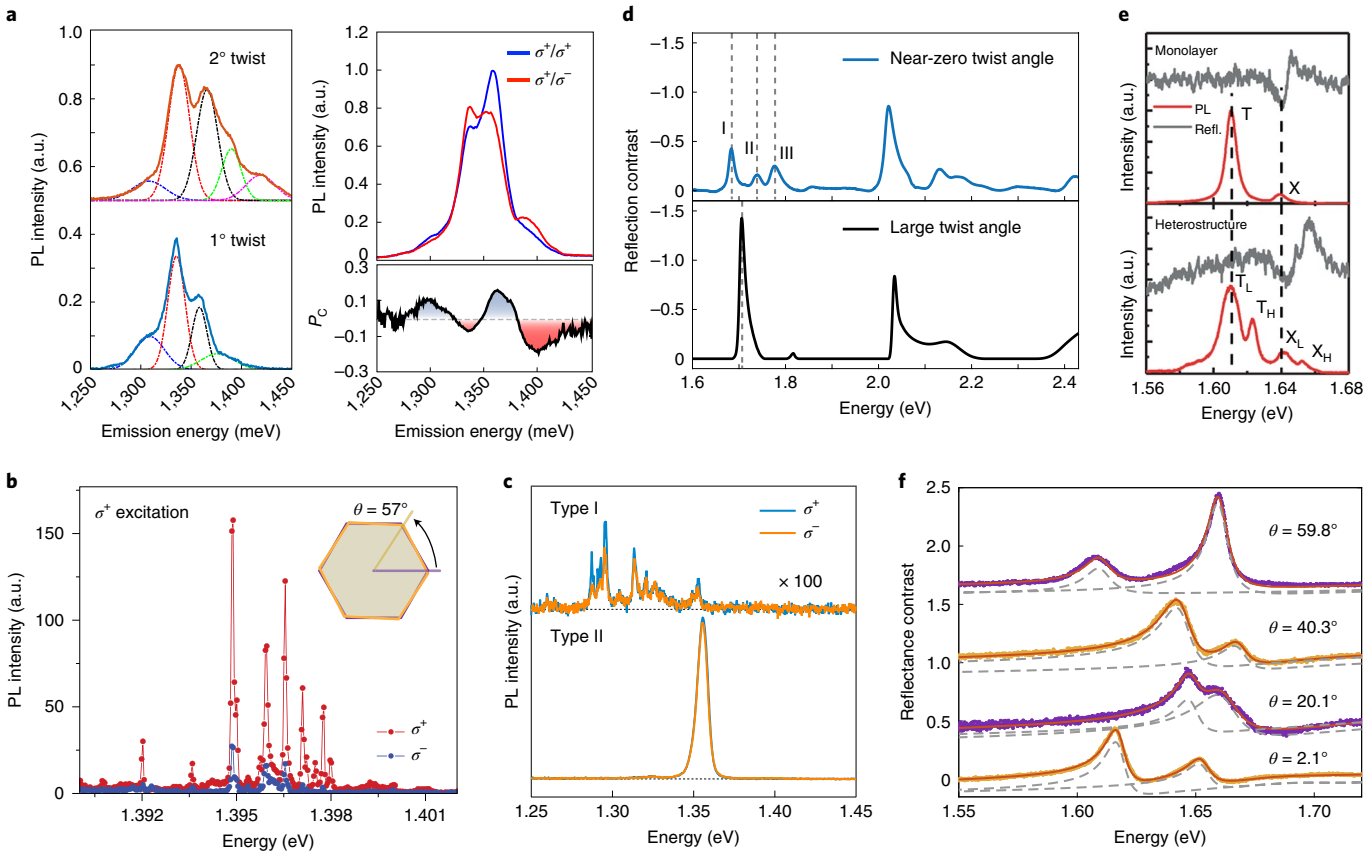

Fig. 3 | Initial experimental evidence of moiré excitons. a, Multiple interlayer exciton resonances in PL observed in 1° and 2° $MoSe_2/WSe_2$ bilayers. Each spectrum is fitted with four (1°) or five (2°) Gaussian functions (dot-dashed lines). The alternating helicity of the PL peaks excited with σ^+ light is shown in the right panel in the 1° bilayer sample. P_C: degree of circular polarization, grey shaded for positive P_C while red shaded for negative P_C. **b**, Sharp interlayer exciton resonances and their helicity observed in twisted $MoSe_2/WSe_2$ bilayers at low excitation density. **c**, Representative PL spectra from two $WSe_2/MoSe_2$ heterobilayer showing sharp resonances (type I) and a broad peak (type II). The blue and orange spectra indicate right (σ^+) and left (σ^-) circularly polarized emission under σ^+ excitation, respectively. The lack of circular emission in type II regions is attributed to uniaxial strain. **d**, Intralayer excitons in twisted WS_2/WSe_2 bilayers observed in reflectance spectra. The 1s exciton state in WSe_2 was observed to split into three peaks (I–III) due to the moiré potential. **e**, Intralayer exciton (X) and trion (T) split into two branches (at lower and higher energy denoted by the subscripts L and H, respectively) in the PL spectrum of twisted $MoS_2/MoSe_2$ bilayers. Refl., reflectance spectrum. **f**, Hybrid excitons in twisted $MoSe_2/WS_2$ bilayers. Here dashed lines are the fitted individual hybrid exciton resonances. Panels adapted with permission from: **a**, ref. [82], Springer Nature Ltd; **c**, ref. [88], Springer Nature Ltd; **d**, ref. [83], Springer Nature Ltd; **e**, ref. [84], American Chemical Society. Panels reproduced with permission from: **b**, ref. [75], Springer Nature Ltd; **f**, ref. [42], Springer Nature Ltd.

and valence band maximum states in near-R- and -H-stacked bilayers are theoretically predicted. Although the calculation shown in Fig. 2g is performed on a different material combination (MoS_2/WS_2)[71], it qualitatively agrees with the experiments on WSe_2 twisted bilayers. The regions with high hole densities in Fig. 2g correspond to blue shades and should be compared to the yellow/bright regions in Fig. 2e,f. Because of the very different energy bands and spatial distribution of the states, one should expect the exciton properties, including the dipole moment and localization, to vary between the R-stacked and H-stacked MSLs[71,80,81]. Bilayers with different chalcogenide atoms, such as WS_2/WSe_2, are expected to exhibit a deeper moiré potential because a larger lattice mismatching leads to a stronger local strain and layer-spacing variations. More accurate STM/S experiments on high-quality samples without extrinsic strain are still needed to confirm such predictions.

Early evidence of moiré excitons

Several groups reported the first experimental evidence of moiré excitons in TMD heterostructures in 2019[41,75,82–84]. These experiments were performed on different combinations of TMD bilayers encapsulated by hBN layers. Because of the improved sample quality and reduced inhomogeneous linewidth, fine structures of exciton resonances were observed and attributed to moiré mini-bands.

Near-commensurate structures, $MoSe_2/WSe_2$ heterobilayers, have been investigated in two early studies that focused on rather different spectroscopy features. Tran and co-workers reported multiple, relatively broad (~10 meV linewidth) interlayer excitons[82]. Two samples with twist angles of ~1° and ~2° were investigated (Fig. 3a). While there were some fluctuations in the peak energies, the spacing between the resonances was larger in the ~2° sample (~27 meV) than that in the ~1° sample (~22 meV). These resonances were attributed to the ground and excited exciton states confined at a global minimum within the moiré supercell. In the simplest model, excitons in the smaller moiré supercell of the 2° sample experience tighter lateral quantum confinement, leading to a larger energy separation between the ground and excited states. This interpretation is based on the alternating circular polarization of the PL signal in the 1° sample (Fig. 3a, right column). The temperature dependence and the shorter lifetimes of the higher energy states provided further evidence that supports this interpretation of multiple interlayer exciton resonances. Similar spectroscopic features have been observed for ground- and excited-state

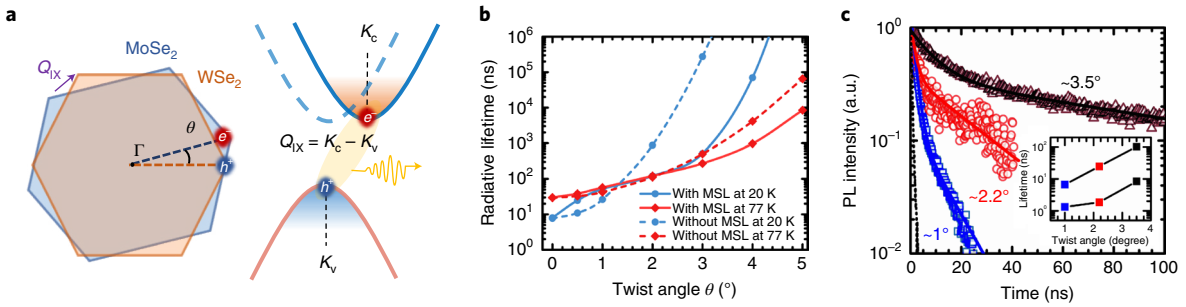

Fig. 4 | Dynamics of moiré excitons. a, A rotation in real space shifts the conduction and valence bands, causing K–K excitons to become an indirect transition in the momentum space. **b**, Calculated interlayer moiré exciton radiative lifetimes with (solid line) and without (dashed lines) the MSL at two different temperatures. **c**, Interlayer exciton lifetime measured in three $MoSe_2/WSe_2$ bilayers with 1°, 2.2° and 3.5° twist angles. Inset presents the extracted fast and slow decay components in the twisted bilayer samples. Panels **a**–**c** adapted with permission from ref. [97], APS.

excitons frequently observed in an ensemble of InAs self-assembled quantum dots[85].

Seyler and co-workers also investigated $MoSe_2/WSe_2$ heterobilayers but focused on narrow resonances with a linewidth of ~80 μeV (Fig. 3b), observable at a lower temperature (~2 K) and lower excitation power (~10–100 nW) compared with those presented in Fig. 3a[75]. Such narrow resonances were observed in the heterobilayers with twist angles of around 2° (R-stacking), 57° (H-stacking) and 20° (incidental commensurate stacking). Upon circularly polarized laser excitation, all observed resonances exhibit circularly polarized PL with the same helicity as the excitation laser in the ~57° and ~20° samples but the opposite helicity in the 2° sample, as illustrated in Fig. 3b. The authors concluded that all resonances in one sample originate from sites with a common interlayer atomic registry and C_3 symmetry. When applying a magnetic field, Zeeman splitting of the exciton resonances yields a large Landé g factor of around −15.8 in both the 57° and 20° twisted bilayers but a reduced Landé g factor of 6.72 with an opposite sign in the 2° sample. It is inferred that the interlayer exciton transitions in the 57° and 20° twisted heterobilayers occur between different valleys, namely from the K (K′) valley in the conduction band of $MoSe_2$ to the K′ (K) valley in the valence band of WSe_2. By contrast, interlayer exciton transitions occur between the same valley in the 2° heterobilayer. This difference originates from the distinct valley alignment in adjacent layers for R- and H-stacked bilayers.

Both sharp resonances[35,60,86–88] and the broader interlayer exciton resonances[60,88–92] have been observed in more recent experiments in the same $MoSe_2/WSe_2$ bilayers. Bai and collaborators observed both a few sharp resonances (labelled as type I in Fig. 3c) and a broad peak (type II in Fig. 3c) that evolved into multiple, broader interlayer exciton resonances with increasing excitation power[60,88]. Piezoresponse force microscopy images revealed that the moiré supercells in some regions were elongated by uniaxial strain leading to linearly polarized, type II emission, analogous to early GaAs quantum dots with an elongated confinement potential[93]. Because the multiple broad resonances emerge at higher excitation densities, the authors attributed these resonances to delocalized states, whereas type I sharp resonances were attributed to zero-dimensional moiré potential traps. However, because hundreds of moiré supercells are simultaneously excited in far-field optical experiments, the type I sharp resonances probably originate from a few selected localization sites within the moiré potential rather than from all excited moiré supercells.

New experiments revealed that the sharp resonances exhibit many characteristic features of single-photon emitters, including antibunching[86], spectral wandering[35] and intensity brightening at sites strained by nanopillars[87]. Strain engineering has been widely applied to brighten single-photon emitters in WSe_2 monolayers and in hBN flakes[94,95], where quantum emitters are attributed to point defects modified by a strain field. Whether or not the moiré potential is the dominant trapping mechanism for excitons in these early spectroscopy experiments on TMD bilayers is still being actively debated. The debates may not be fully resolved until experiments that are capable of probing individual moiré excitons are performed using an optical near-field technique or tip-induced luminescence in STM.

Moiré excitons have also been observed in incommensurate heterobilayers, such as WS_2/WSe_2 and $WS_2/MoSe_2$. Because the supercell size is smaller for the same twist angle in these incommensurate MSLs, one may expect stronger lateral confinement. Jin et al. reported the splitting of an intralayer WSe_2 A exciton into multiple peaks in a WS_2/WSe_2 heterobilayer with a twist angle smaller than 3° (ref. [83]). By contrast, such multiple resonances are absent in a bilayer with a large twist angle (Fig. 3d). The split resonances were observed both in R- and H-stacked heterobilayers in both reflectance and PL excitation spectra, indicating similarly large dipole moments as intralayer excitons in a monolayer. Zhang et al. (Fig. 3e)[84] reported additional neutral exciton and trion resonances in a $MoSe_2/MoS_2$ heterobilayer with an approximately 1° twist angle. On the basis of the observation that these new peaks disappeared at ~90 K, they estimated that the depth of the moiré potential for the intralayer excitons was ~26 meV. This value should not be confused with the deep moiré potential depth extracted from STM experiments that measure the single-particle bands at the high-symmetry points. The effective moiré potential experienced by the intralayer excitons is shallower than that by the interlayer excitons, which is influenced by the type II band alignment[50,71].

Hybrid excitons in $MoSe_2/WS_2$ heterobilayers were reported by Alexeev et al.[41] and Zhang et al.[42] In a series of samples with near-R-, -H- or other incidentally commensurate bilayers, multiple resonances that exhibit a systematic change in the energy splitting and relative intensity between the hybridized excitons enabled the effective mass and electron interlayer tunnelling to be extracted, as shown in Fig. 3f. Tang et al. further revealed the strong interaction between intralayer and interlayer excitons in WSe_2/WS_2 and $MoSe_2/WS_2$ heterobilayers[40], by observing the anti-crossing phenomenon between hybridized exciton states when an electric field and carrier density were used to tune the resonant energies.

Twist-angle-dependent exciton dynamics and diffusion

A large range of interlayer exciton lifetimes (from around one nanosecond to microseconds) has been reported in early experiments[22,32,64,66,96]. It has been recognized recently that not only the resonant energies but also the quantum dynamics of excitons are controllable via the twist angle. Measurements on several $MoSe_2/WSe_2$ bilayers have found that the interlayer exciton lifetime

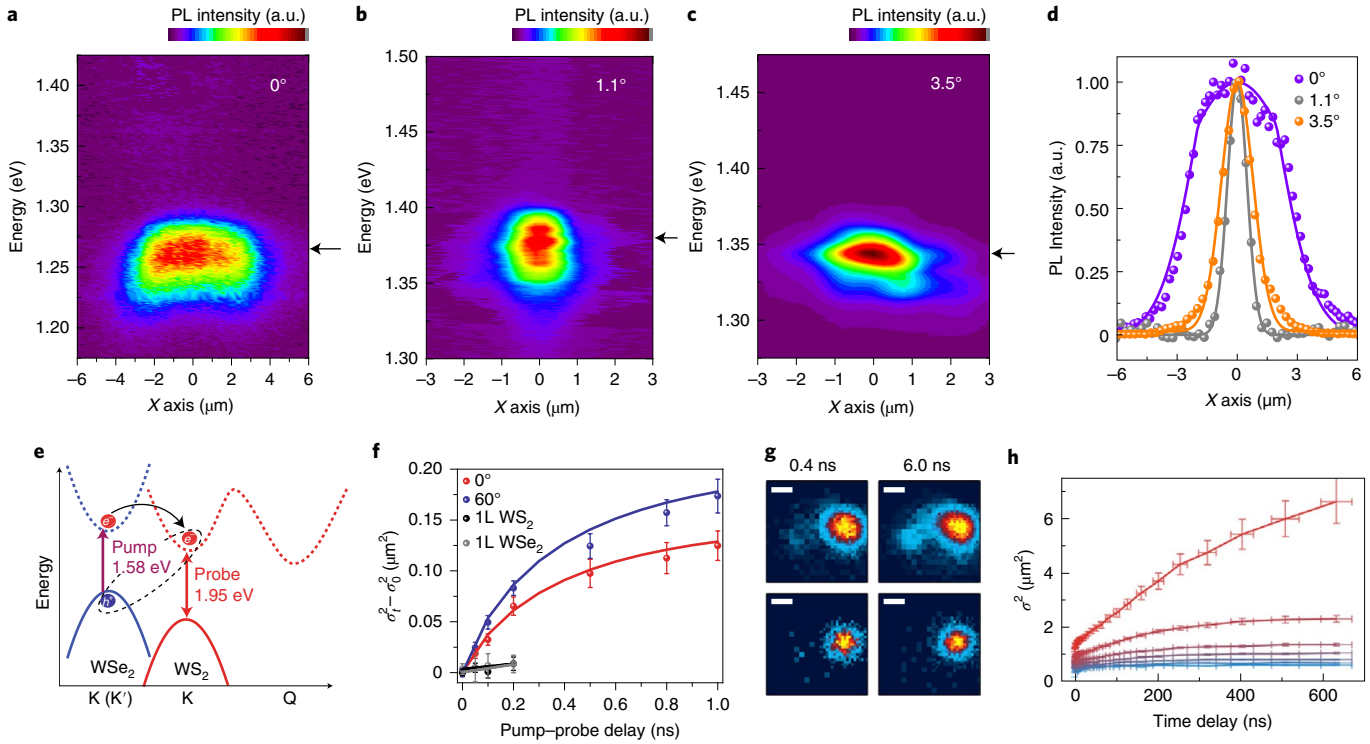

Fig. 5 | Spatial diffusion of moiré excitons. a–c, 2D PL images and spectra of interlayer excitons with the spatial (energy) coordinate shown in the horizontal (vertical) axis in 0° (**a**), 1.1° (**b**) and 3.5° (**c**) twisted $MoSe_2/WSe_2$ heterobilayer. **d**, Line profile of moiré exciton diffusion for the samples in **a–c**. The photon energies for these profiles are indicate by the black arrows in **a–c**. **e**, Schematic of a pump–probe microscopy experiment probing exciton diffusion in CVD-grown WSe_2/WS_2 bilayers. **f**, Using pump–probe experiments described in **e**, different exciton diffusion profiles are found in R- and H-stacked bilayers that change as a function of the delay. 1L, monolayer. Error bars indicate the uncertainty of the diffusion profiles. **g**, PL images at two different time delays for high ($9.3\times10^{13}\,cm^{-2}$; upper panels) and low ($1.3\times10^{12}\,cm^{-2}$; lower panels) excitation densities. Scale bar, 2 μm. **h**, Time-dependent spatial variance σ^2 as a function of delay at different exciton densities. Error bars indicate the uncertainty of the time dealy (X-axis) and the spatial variance (Y-axis). Panels adapted with permission from: **a–c**, ref. [105], AAAS under a Creative Commons license CC BY 4.0; **g**,**h**, ref. [60], APS. Panels **e**,**f** reproduced with permission from ref. [106], Springer Nature Ltd.

changes by one order of magnitude when the twist angle is changed from 1° to 3.5° (ref. [97]). Two mechanisms contribute to such pronounced twist-angle-dependent dynamics. First, a larger twist angle in real space translates into a rotation in momentum space and a larger MBZ (Fig. 4a). Consequently, valleys in each layer are shifted relative to each other, changing the direct K–K exciton transition to an indirect transition. This momentum mismatch of $Q_{IX} = K_c - K_v$ (where IX denotes the interlayer exciton, and K_c and K_v are the momentum of electrons in the conduction band and holes in the valence-band which form the interlayer excitons) gives rise to a finite exciton centre-of-mass momentum, and leading to a longer radiative lifetime for the interlayer excitons. Second, the periodic energy modulation of the moiré potential softens the twist-angle dependence. Qualitatively, the moiré potential relaxes the momentum conservation between the interlayer excitons and photons, thus opening more radiative decay channels. In addition to the twist-angle dependence, temperature-dependent radiative lifetimes were predicted. The calculated interlayer exciton radiative lifetimes at two different temperatures are shown in Fig. 4b. In a MSL with a larger twist angle, a thermally broadened exciton distribution increases the overlap with the light cone and facilitates radiative decay.

Choi et al. reported lifetimes of multiple interlayer excitons attributed to the ground and excited states confined by the moiré potential in several $MoSe_2/WSe_2$ MSLs with controlled twist angles[97]. Taking into account the expected energy shift from moiré supercell confinement, the lifetimes of the first excited state were found to increase by approximately one order of magnitude in the 3.5° MSL compared with the 1° MSL (Fig. 4c). The predicted temperature-dependent lifetimes of moiré excitons were also validated in these experiments. In practice, this twist-angle-dependent lifetime measurement can be used to estimate and compare the twist angle of a series of MSLs with higher sensitivity than the polarization-resolved second harmonic generation technique that is commonly used.

Furthermore, understanding the multiple decay times often observed in PL (Fig. 4c) or the pump/probe dynamics of interlayer excitons[91,97] requires a model that takes into account other states beyond the bright excitons. While only emissions from bright excitons are detected in PL experiments, any processes that repopulate the bright exciton states can lead to multiple decay times, for example, dark-to-bright exciton conversions or valley-indirect to valley-direct exciton conversions[98]. To fully resolve these processes experimentally, more advanced spectroscopy tools are needed, such as time- and angle-resolved photoemission spectroscopy experiments[99–101].

Whether or not excitons are localized within moiré supercells is an important fundamental question with great implications for applications. For example, a regular array of localized excitons may find exciting applications in quantum information science as quantum emitters with tunable chirality[13,50,94,95]. While most early experiments have suggested a long diffusion length for interlayer excitons in TMD bilayers[96,102,103], they are probably localized within moiré supercells if the potential is sufficiently deep and the supercell size

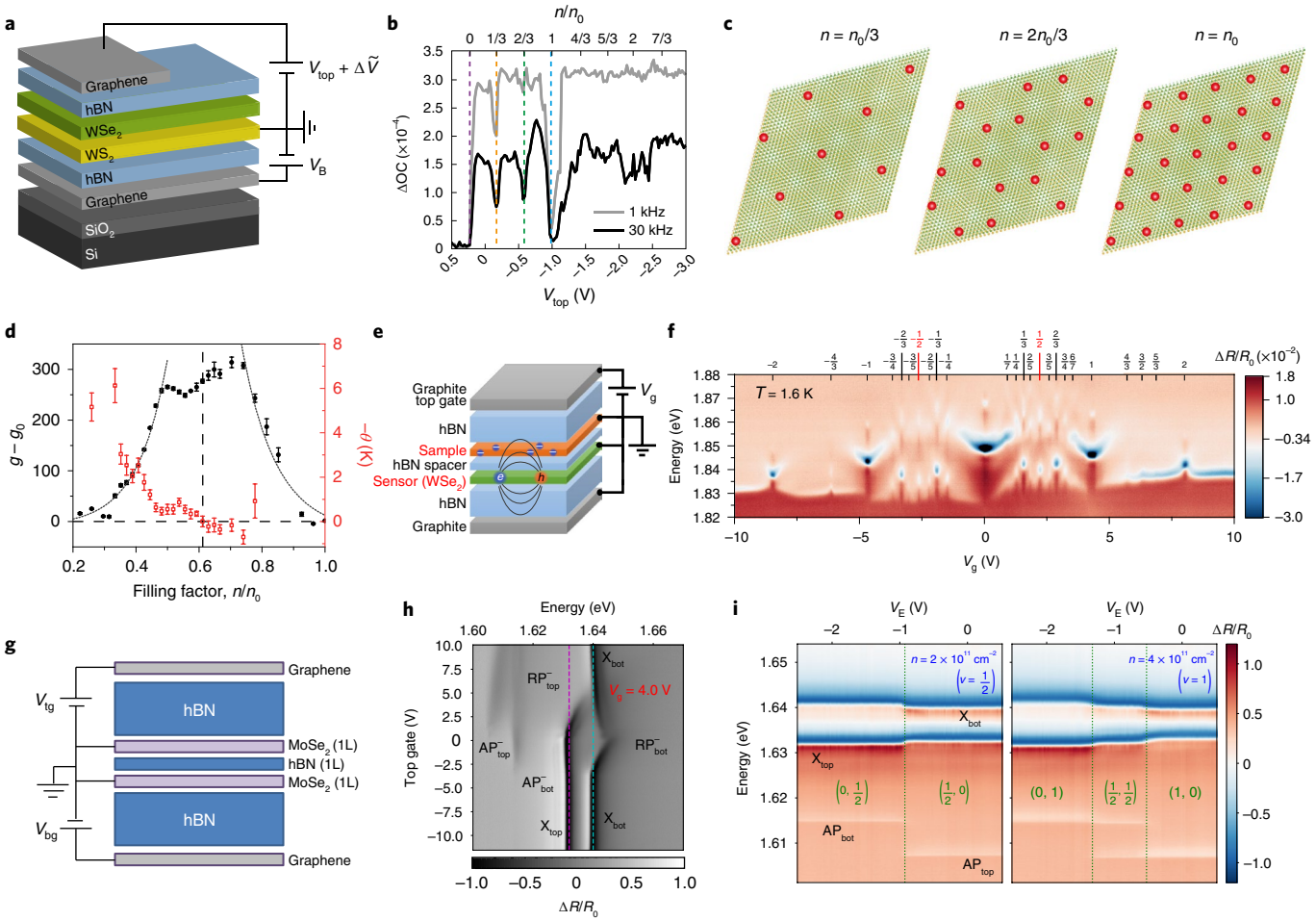

Fig. 6 | Experimental evidence of the correlated electron states probed by excitons. a,**b**, A near-0° WS_2/WSe_2 heterobilayer device (**a**) used to observe the Mott insulating state ($n=n_0$; blue dashed line) and Wigner crystal states ($n=1/3n_0$ and $n=2/3n_0$; yellow and green dashed lines, respectively) in optical reflectance (**b**) with the electron density n tuned to a fraction of the moiré supercell density n_0. V_B, back-get voltage; $\Delta\tilde{V}$, a.c. excitation voltage; ΔOC, optical contrast; V_{top}, top-gate voltage. **c**, Illustrations of generalized Wigner crystal ($n=1/3n_0$ and $n=2/3n_0$; left and middle, respectively) and Mott insulator ($n=n_0$; right) states in a WSe_2/WS_2 MSL. Red spheres indicate the localized charges in the doped MSL. **d**, Antiferromagnetic interaction inferred in a near-0°-twisted WS_2/WSe_2 bilayer via the exciton Zeeman splitting in a magnetic field. Here, $n_0/2$ is the density of moiré supercells. $g-g_0$, difference of Landé g-factor between excitons in the MSL and bare excitons, data shown in filled black circles; θ, Weiss constant, data in open red squares. Error bars for $g-g_0$ and θ are uncertainties obtained from the curve fittings to the data in ref. [8]. **e**,**f**, Nearly two dozen correlated insulating states reported in a WSe_2/WS_2 bilayer (**f**) using the device illustrated (**e**). These insulating states were detected via the 2*s* exciton of a separate WSe_2 sensor layer. V_g, gate voltage; $\Delta R/R_0$, gate-dependent reflection contrast. **g**, An MSL consisting of two $MoSe_2$ monolayers separated by a monolayer hBN spacer. V_{tg}, top-gate voltage; V_{bg}, bottom-gate voltage. **h**, As a function of the top-gate voltage, repulsive polarons in the bottom layer show non-monotonic spectral shifts. Magenta and cyan dashed lines indicate the top (E = 1.632 eV) and bottom (E = 1.640 eV) exciton resonance energies, respectively. $X_{top/bot}$, top/bottom layer excitons; $AP^-_{top/bot}$, top/bottom layer attractive polarons; $RP^-_{top/bot}$, top/bottom layer repulsive polarons. **i**, At two different total doping levels (denoted by n), electrons collectively transfer from one to the other layer manifested as stepwise spectral shifts and attributed to electron incompressibility. $V_E = 0.5V_{tg} - 0.5V_{bg}$, which tunes the vertical electrical field across the heterostructure; ν, filling factor; $AP_{top/bot}$, top/bottom layer attractive polarons. Green dashed lines indicate threshold V_E for incompressible carrier transfer between the top and bottom layers. Panels adapted with permission from: **a**–**c**, ref. [111], Springer Nature Ltd; **g**–**i**, ref. [10], Springer Nature Ltd. Panels reproduced with permission from: **d**, ref. [8], Springer Nature Ltd; **e**,**f**, ref. [9], Springer Nature Ltd.

is 2–20 times that of the exciton Bohr radius. If the supercells are too large, excitons essentially experience a 2D potential. If the supercell is too small, on the other hand, the picture of a bound electron–hole pair moving in a smooth potential breaks down[104].

Recently, Choi et al. compared interlayer exciton diffusion in several $WSe_2/MoSe_2$ heterostructures using steady-state PL mapping[105]. A CVD-grown $WSe_2/MoSe_2$ heterostructure forms a commensurate structure, that is, no moiré lattice is present. In such a sample, a long exciton diffusion length of ~10 μm was observed (Fig. 5a). In this sample, the interlayer exciton diffusion was truncated by the boundary of the heterostructure as evidenced by an abrupt drop in signal. In a stacked 1.1° bilayer (Fig. 5b), no evidence of exciton diffusion beyond the optical diffraction limit was found at either low or high excitation density under the continuous-wave laser excitation.

In the ~3.5° twisted bilayer, interlayer exciton diffusion became observable, especially at high excitation densities (Fig. 5c). A direct comparison between the diffusion lengths in these samples is displayed in Fig. 5d. The observed twist-angle-dependent exciton diffusion is consistent with a recent theoretical study that calculated exciton dispersion in $WSe_2/MoSe_2$ bilayers[104]. The flat exciton dispersion for a 1.1° twisted bilayer indicates spatial localization.

By contrast, the calculated exciton dispersion changed notably for a 3.5° twisted bilayer, which is consistent with delocalized excitons. In addition, because the diffusion length L is related to the lifetime τ via $L = \sqrt{D\tau}$, one should expect the diffusion length to depend on the twist angle as well. It is difficult to accurately determine the diffusion coefficient, D. The wide range of values for D in the literature arises partially because different models and methods have been used to analyse diffusion data. Exciton resonances at higher energies are predicted to be more mobile than those at lower energies[104], although this energy-dependent diffusion has yet to be demonstrated.

Beyond steady-state PL experiments, ultrafast non-linear experiments have been used to investigate exciton diffusion in CVD-grown, rotationally aligned WS_2/WSe_2 heterobilayer with both R- and H-stacking[106]. The pump laser was tuned to the intralayer exciton energy of WSe_2 (1.58 eV) while the probe wavelength was tuned near the intralayer exciton energy of WS_2 (1.95 eV). The rapid charge transfer in the type II heterostructures allows one to probe non-linear signals from either the electron in WS_2 or interlayer excitons, as illustrated in Fig. 5e. With improved temporal and spatial resolutions, these experiments demonstrated convincingly that the carrier or exciton diffusion coefficients are modified by the stacking order, temperature and exciton density (Fig. 5f).

In another time-resolved PL experiment, Wang et al. investigated mechanically stacked, non-commensurate R-stacked $MoSe_2/WS_2$ heterobilayers and focused on density-dependent transitions of the moiré exciton phases[60]. The localized interlayer excitons trapped by the moiré potential evolve into a free exciton gas and electron/hole plasma as the excitation density increases (Fig. 5g,h). At high exciton density ($>1\times10^{13}\,cm^{-2}$), a dynamic change of the diffusion coefficient reveals that the exciton distribution expands rapidly in the first 10 ns due to the strong initial Coulomb repulsion. The diffusion coefficient then stabilizes between 10 and 100 ns, indicating diffusive exciton transport. Subsequently, the diffusion coefficient drops further, suggesting that excitons are trapped by the moiré potential again at low density. The evolution of the localized, mobile and ionized phases of moiré excitons are concurrent with the notable changes in linewidth and centre wavelength of PL in both the temporal and spatial domains.

Correlated electronic phases probed by optical spectroscopy

The low-energy electrons in both graphene and TMD-based MSLs can be described using continuum models[79,107,108]. The single-particle eigenstates are calculated using a Hamiltonian with its dimension determined by the number of low-energy bands. In twisted graphene bilayers, sixteen bands are needed to account for the four triangular sublattice pseudospins, spin and valley degrees of freedom. In the case of twisted TMD heterobilayers, only two low-energy valence bands need to be taken into account when the chemical potential is within the topmost valence band. Its Hamiltonian can be mapped to a single-band Hubbard model. Thus, TMD MSLs have been proposed as a new solid-state platform to simulate the Hubbard model with the unprecedented advantage that both the bandwidth and interaction strength are widely tunable[79,109,110].

Most relevant to this Review, optical spectroscopy measurements featuring excitonic resonances have been used to probe correlated electron states, complementary to the transport measurements[8–10,111–113]. The pioneering studies on WSe_2/WS_2 MSLs with near-zero twist angles by Regan et al.[111] and Tang et al.[8] investigated similar vertically stacked devices (Fig. 6a) in which the hole density in the WSe_2 layer is tuned. An insulating state attributed to the Mott insulating state at half-filling of the moiré supercell (that is, one hole per supercell) was found in transport measurements and was observed to be concurrent with an increased reflectance at the exciton resonance. Regan et al. reported additional insulating states at 1/3 and 2/3 of the 'half-filling' states, as shown in Fig. 6b. These states were attributed to generalized Wigner crystal states accompanied by the formation of charge density waves as illustrated in Fig. 6c. Tang et al. also investigated the magnetic interaction between holes localized by the moiré potential[8]. The magnetic susceptibility was extracted from the Zeeman splitting between intralayer excitons at various temperatures and doping levels under an out-of-plane magnetic field (Fig. 6d). A negative Curie temperature was extrapolated from the magnetic susceptibility as a function of the temperature, and it was interpreted as evidence for an antiferromagnetic interaction between the localized holes. The extrapolated magnetic ordering temperature lies well below the accessible temperature range in the experiments.

By placing a WSe_2 monolayer separated by ~1 nm hBN from the WSe_2/WS_2 MSL (Fig. 6e), Xu et al. reported nearly two dozen correlated insulating states at various fractional filling values[9] (Fig. 6f). This experiment relied on the energy shift of the excited-state excitons (for example, the 2*s* state) with a larger Bohr radius than that of the 1*s* exciton, acting as a sensitive probe of correlated electrons in the spatially separated MSL[114–116]. In some cases, these insulating states were attributed to generalized Wigner crystal states and charge density waves. The signatures of such abundant correlated insulating states in TMD MSLs were also reported from scanning probe spectroscopy, capacitance measurements and PL experiments on WSe_2/WS_2 MSLs[11,12,117,118].

A very different type of MSL was explored by Shimazaki et al.[10]. A thin hBN layer was inserted between two twisted $MoSe_2$ monolayers to control the carrier tunnelling as shown in Fig. 6g. The moiré potential was very shallow, estimated to be only several millielectronvolts according to the first-principles calculations[10]. The presence of itinerant carriers dresses the excitons to form attractive and repulsive polarons, which are identified by two branches in the reflectance spectrum as a function of the doping. Negative compressibility was found at specific back-gate voltages, that is, a counterintuitive depletion of itinerant charges in the bottom layer when the top-gate voltage was increased (Fig. 6h). Incompressible correlated electron states were observed when the doping level was an integer multiple of $n_{moiré}$, as shown in Fig. 6i, where $n_{moiré}$ is the density of the moiré supercells. At these doping levels, a collective charge transfer between the top and bottom layers occurred in a stepwise fashion, that is, $n_{moiré}$, $2n_{moiré}$ and so on. These two phenomena related to compressibility occurred to minimize the global electron energy in both the top and bottom layers.

Zhou et al. investigated a similar $MoSe_2/hBN/MoSe_2$ heterostructure with a 1 nm hBN spacer layer[112]. When both the top and bottom layer were tuned to the *n*-doped regime over a limited gate voltage range, an enhancement of the exciton resonance in both the PL and reflectance spectra was observed when the doping density ratio between the top- and bottom-layer $MoSe_2$ was 1:1, 4:1, 7:1 and 1:4. This result was attributed to the formation of a Wigner crystal in a triangular electron lattice hosted in each layer, which was stabilized by the interlayer interaction.

Concluding remarks

Moiré excitons represent just one topic of interest in the new physics and opportunities presented by MSLs. It draws from the extensive earlier knowledge of conventional semiconductor heterostructures such as III–V quantum wells and quantum dots[119–121]. Even within the topic of moiré excitons, we have mostly focused on optical spectroscopy experiments, which only probe dipole-allowed, bright excitons directly. This field is still far from mature and is confronted with many debates and challenges. We summarize some of these challenges here.

Mapping moiré potential and establishing the link to moiré excitons. The moiré potential in different MSLs depends on several factors including material combinations, stacking orders, twist angles

and strain (either intrinsic or extrinsic). Even for the same combination of bilayers, the sequence of stacking on the substrate may change the local interlayer spacing and stacking style[54]. Previous studies often assume that the moiré potential depth does not change as a function of twist angle and that a rigid lattice model applies in TMD bilayers. These assumptions have been challenged by recent experiments[81]. Lattice reconstructions are known to exist in twisted bilayers of graphene and TMDs[44,46,69,122–124]. Recent microscopy and Raman spectroscopy measurements have shown that such lattice reconstructions occur over a notably larger range of twist angles in TMD homobilayers than that found in graphene bilayers[49]. The lattice reconstruction has an essential impact on electronic bands, and their influence on optical properties has just begun to be explored[44]. Theoretically, electrons, holes and excitons are predicted to localize at different locations in the real space within the moiré supercells. Experiments with sufficient spatial and momentum resolution to map such charge distributions have just begun to emerge[125]. Optical experiments that can explicitly probe the locations of moiré excitons are more challenging.

Optical spectroscopy of moiré excitons. We would like to remind readers that all optical experiments reporting on moiré excitons in TMD heterostructures have so far been performed in the far-field limit, in which ~1,000 moiré supercells are probed simultaneously. Without isolating an individual moiré supercell, pinpointing the role of the moiré potential is challenging due to the presence of spatial inhomogeneity and defects. One should keep in mind that the interpretations of early experiments presented in this Review are still rapidly evolving. Techniques that are capable of simultaneously imaging the supercells, evaluating the moiré potential and correlated states via optical spectroscopy measurements will be very valuable to advance our understanding. Promising techniques include but are not limited to near-field scanning optical microscopy, cathodoluminescence and STM tip-induced luminescence. Future studies based on these techniques with high spatial resolution will eliminate some ambiguity, either validating or challenging the assumptions made when interpreting the early experiments. Progress along these directions has been reported recently[126].

Correlated states in MSLs. There are still many open theoretical and experimental questions regarding correlated states in TMD MSLs. The finding that optical spectroscopy can be used to probe correlated ground states is somewhat surprising. It has been argued that the correlated states change the dielectric screening and consequently modify the exciton resonances observed in optical spectroscopy. The microscopic mechanisms of how correlated electrons interact with excitons have yet to be fully investigated. Some ambiguity on the filling factors remains in the absence of standard Hall bar measurements. The number and filling fractions of the insulating states observed in each sample and experiment exhibit unexplained variations[127,128]. The nature of the insulating states (Mott insulators or charge-transfer insulators) observed at half-filling is still under debate[107,128–130]. The emergence of correlated electronic states in twisted $MoSe_2$ bilayers with an hBN spacer layer warrants further investigation given the shallow moiré potential[131].

Considering TMD MSLs as either designed correlated materials or quantum simulation platforms links the field of vdW materials to broader communities that have been investigating correlated materials over several decades. Almost all early experiments on correlated states in TMD MSLs have been performed in the classical limit of zero tunnelling between adjacent moiré supercells. These experiments undoubtedly suggest an exciting direction of probing correlated electron states via optical spectroscopy experiments, where many opportunities for discoveries have yet to be explored[132].

Platform for new materials. By removing the requirement of matching lattice constants, the choice of materials in constructing a vdW heterostructure is drastically expanded. We have only reviewed recent studies on MSLs based on the most commonly studied TMDs. New materials including vdW ferroelectric and magnetic materials are emerging. These materials can be used to create ferroelectric or magnetic MSLs with controlled domains[133–136]. They can also be combined with semiconductor MSLs. With more diverse and advanced MSLs quickly emerging[137,138], we fully expect MSLs to remain an exciting platform for probing electronic and photonic quantum phenomena over the next decade.

Received: 30 April 2021; Accepted: 6 December 2021;
Published online: 14 March 2022

References

1. Bistritzer, R. & MacDonald, A. H. Moiré bands in twisted double-layer graphene. *Proc. Natl Acad. Sci. USA* **108**, 12233–12237 (2011).
2. Cao, Y. et al. Unconventional superconductivity in magic-angle graphene superlattices. *Nature* **556**, 43–50 (2018).
3. Cao, Y. et al. Correlated insulator behaviour at half-filling in magic-angle graphene superlattices. *Nature* **556**, 80–84 (2018).
4. Kerelsky, A. et al. Maximized electron interactions at the magic angle in twisted bilayer graphene. *Nature* **572**, 95–100 (2019).
5. Lu, X. et al. Superconductors, orbital magnets and correlated states in magic-angle bilayer graphene. *Nature* **574**, 653–657 (2019).
6. Choi, Y. et al. Correlation-driven topological phases in magic-angle twisted bilayer graphene. *Nature* **589**, 536–541 (2021).
7. Wang, L. et al. Correlated electronic phases in twisted bilayer transition metal dichalcogenides. *Nat. Mater.* **19**, 861–866 (2020).
8. Tang, Y. et al. Simulation of Hubbard model physics in WSe_2/WS_2 moiré superlattices. *Nature* **579**, 353–358 (2020).
9. Xu, Y. et al. Correlated insulating states at fractional fillings of moiré superlattices. *Nature* **587**, 214–218 (2020).
10. Shimazaki, Y. et al. Strongly correlated electrons and hybrid excitons in a moiré heterostructure. *Nature* **580**, 472–477 (2020).
11. Huang, X. et al. Correlated insulating states at fractional fillings of the WS_2/WSe_2 moiré lattice. *Nat. Phys.* **17**, 715–719 (2021).
12. Chu, Z. et al. Nanoscale conductivity imaging of correlated electronic states in WSe_2/WS_2 moiré superlattices. *Phys. Rev. Lett.* **125**, 186803 (2020).
13. Naik, M. H., Kundu, S., Maity, I. & Jain, M. Origin and evolution of ultraflat bands in twisted bilayer transition metal dichalcogenides: realization of triangular quantum dots. *Phys. Rev. B* **102**, 075413 (2020).
14. Zhao, X.-J., Yang, Y., Zhang, D.-B. & Wei, S.-H. Formation of Bloch flat bands in polar twisted bilayers without magic angles. *Phys. Rev. Lett.* **124**, 086401 (2020).
15. Splendiani, A. et al. Emerging photoluminescence in monolayer MoS_2. *Nano Lett.* **10**, 1271–1275 (2010).
16. He, K. et al. Tightly bound excitons in monolayer WSe_2. *Phys. Rev. Lett.* **113**, 026803 (2014).
17. Chernikov, A. et al. Exciton binding energy and nonhydrogenic Rydberg series in monolayer WS_2. *Phys. Rev. Lett.* **113**, 076802 (2014).
18. Tartakovskii, A. Excitons in 2D heterostructures. *Nat. Rev. Phys.* **2**, 8–9 (2020).
19. Rivera, P. et al. Interlayer valley excitons in heterobilayers of transition metal dichalcogenides. *Nat. Nanotechnol.* **13**, 1004–1015 (2018).
20. Tran, K., Choi, J. & Singh, A. Moiré and beyond in transition metal dichalcogenide twisted bilayers. *2D Mater.* **8**, 022002 (2021).
21. Yu, Y. et al. Equally efficient interlayer exciton relaxation and improved absorption in epitaxial and nonepitaxial MoS_2/WS_2 heterostructures. *Nano Lett.* **15**, 486–491 (2015).
22. Rivera, P. et al. Observation of long-lived interlayer excitons in monolayer $MoSe_2$–WSe_2 heterostructures. *Nat. Commun.* **6**, 6242 (2015).
23. Jin, C. et al. Ultrafast dynamics in van der Waals heterostructures. *Nat. Nanotechnol.* **13**, 994–1003 (2018).
24. Kang, J., Tongay, S., Zhou, J., Li, J. & Wu, J. Band offsets and heterostructures of two-dimensional semiconductors. *Appl. Phys. Lett.* **102**, 012111 (2013).
25. Guo, Y. & Robertson, J. Band engineering in transition metal dichalcogenides: stacked versus lateral heterostructures. *Appl. Phys. Lett.* **108**, 233104 (2016).
26. Zhang, C. et al. Systematic study of electronic structure and band alignment of monolayer transition metal dichalcogenides in van der Waals heterostructures. *2D Mater.* **4**, 015026 (2016).

27. Ceballos, F., Bellus, M. Z., Chiu, H. & Zhao, H. Ultrafast charge separation and indirect exciton formation in a MoS_2–$MoSe_2$ van der Waals heterostructure. *ACS Nano* **8**, 12717–12724 (2014).
28. Hong, X. et al. Ultrafast charge transfer in atomically thin MoS_2/WS_2 heterostructures. *Nat. Nanotechnol.* **9**, 682–686 (2014).
29. Zheng, Q. et al. Phonon-assisted ultrafast charge transfer at van der Waals heterostructure interface. *Nano Lett.* **17**, 6435–6442 (2017).
30. Li, Y. et al. Ultrafast interlayer electron transfer in incommensurate transition metal dichalcogenide homobilayers. *Nano Lett.* **17**, 6661–6666 (2017).
31. Gong, Y. et al. Vertical and in-plane heterostructures from WS_2/MoS_2 monolayers. *Nat. Mater.* **13**, 1135–1142 (2014).
32. Miller, B. et al. Long-lived direct and indirect interlayer excitons in van der Waals heterostructures. *Nano Lett.* **17**, 5229–5237 (2017).
33. Nayak, P. K. et al. Probing evolution of twist-angle-dependent interlayer excitons in $MoSe_2$/WSe_2 van der Waals heterostructures. *ACS Nano* **11**, 4041–4050 (2017).
34. Jin, C. et al. On optical dipole moment and radiative recombination lifetime of excitons in WSe_2. *Adv. Funct. Mater.* **27**, 1601741 (2017).
35. Li, W., Lu, X., Dubey, S., Devenica, L. & Srivastava, A. Dipolar interactions between localized interlayer excitons in van der Waals heterostructures. *Nat. Mater.* **19**, 624–629 (2020).
36. Leisgang, N. et al. Giant Stark splitting of an exciton in bilayer MoS_2. *Nat. Nanotechnol.* **15**, 901–907 (2020).
37. Förg, M. et al. Cavity-control of interlayer excitons in van der Waals heterostructures. *Nat. Commun.* **10**, 3697 (2019).
38. Alexeev, E. M. et al. Imaging of interlayer coupling in van der Waals heterostructures using a bright-field optical microscope. *Nano Lett.* **17**, 5342–5349 (2017).
39. Ruiz-Tijerina, D. A. & Fal'ko, V. I. Interlayer hybridization and moiré superlattice minibands for electrons and excitons in heterobilayers of transition-metal dichalcogenides. *Phys. Rev. B* **99**, 125424 (2019).
40. Tang, Y. et al. Tuning layer-hybridized moiré excitons by the quantum-confined Stark effect. *Nat. Nanotechnol.* **16**, 52–57 (2021).
41. Alexeev, E. M. et al. Resonantly hybridized excitons in moiré superlattices in van der Waals heterostructures. *Nature* **567**, 81–86 (2019).
42. Zhang, L. et al. Twist-angle dependence of moiré excitons in WS_2/$MoSe_2$ heterobilayers. *Nat. Commun.* **11**, 5888 (2020).
43. Brem, S. et al. Hybridized intervalley moiré excitons and flat bands in twisted WSe_2 bilayers. *Nanoscale* **12**, 11088–11094 (2020).
44. Andersen, T. I. et al. Excitons in a reconstructed moiré potential in twisted WSe_2/WSe_2 homobilayers. *Nat. Mater.* **20**, 480–487 (2021).
45. Scuri, G. et al. Electrically tunable valley dynamics in twisted WSe_2/WSe_2 bilayers. *Phys. Rev. Lett.* **124**, 217403 (2020).
46. Weston, A. et al. Atomic reconstruction in twisted bilayers of transition metal dichalcogenides. *Nat. Nanotechnol.* **15**, 592–597 (2020).
47. Sung, J. et al. Broken mirror symmetry in excitonic response of reconstructed domains in twisted $MoSe_2$/$MoSe_2$ bilayers. *Nat. Nanotechnol.* **15**, 750–754 (2020).
48. Paradisanos, I. et al. Controlling interlayer excitons in MoS_2 layers grown by chemical vapor deposition. *Nat. Commun.* **11**, 2391 (2020).
49. Quan, J. et al. Phonon renormalization in reconstructed MoS_2 moiré superlattices. *Nat. Mater.* **20**, 1100–1105 (2021).
50. Yu, H., Liu, G.-B., Tang, J., Xu, X. & Yao, W. Moiré excitons: from programmable quantum emitter arrays to spin–orbit-coupled artificial lattices. *Sci. Adv.* **3**, e1701696 (2017).
51. Li, H. et al. Imaging moiré flat bands in three-dimensional reconstructed WSe_2/WS_2 superlattices. *Nat. Mater.* **20**, 945–950 (2021).
52. Wu, F., Lovorn, T. & MacDonald, A. H. Theory of optical absorption by interlayer excitons in transition metal dichalcogenide heterobilayers. *Phys. Rev. B* **97**, 035306 (2018).
53. Shabani, S. et al. Deep moiré potentials in twisted transition metal dichalcogenide bilayers. *Nat. Phys.* **17**, 720–725 (2021).
54. Zhang, C. et al. Interlayer couplings, moiré patterns, and 2D electronic superlattices in MoS_2/WSe_2 hetero-bilayers. *Sci. Adv.* **3**, e1601459 (2017).
55. Ding, Y. et al. First principles study of structural, vibrational and electronic properties of graphene-like MX_2 (M = Mo, Nb, W, Ta; X = S, Se, Te) monolayers. *Physica B* **406**, 2254–2260 (2011).
56. He, J., Hummer, K. & Franchini, C. Stacking effects on the electronic and optical properties of bilayer transition metal dichalcogenides MoS_2, $MoSe_2$, WS_2, and WSe_2. *Phys. Rev. B* **89**, 075409 (2014).
57. Enaldiev, V. V., Zólyomi, V., Yelgel, C., Magorrian, S. J. & Fal'ko, V. I. Stacking domains and dislocation networks in marginally twisted bilayers of transition metal dichalcogenides. *Phys. Rev. Lett.* **124**, 206101 (2020).
58. Zeller, P. & Günther, S. What are the possible moiré patterns of graphene on hexagonally packed surfaces? Universal solution for hexagonal coincidence lattices, derived by a geometric construction. *New J. Phys.* **16**, 083028 (2014).
59. Zeller, P., Ma, X. & Günther, S. Indexing moiré patterns of metal-supported graphene and related systems: strategies and pitfalls. *New J. Phys.* **19**, 013015 (2017).
60. Wang, J. et al. Diffusivity reveals three distinct phases of interlayer excitons in $MoSe_2$/WSe_2 heterobilayers. *Phys. Rev. Lett.* **126**, 106804 (2021).
61. Kunstmann, J. et al. Momentum-space indirect interlayer excitons in transition-metal dichalcogenide van der Waals heterostructures. *Nat. Phys.* **14**, 801–805 (2018).
62. Hsu, W.-T. et al. Negative circular polarization emissions from WSe_2/$MoSe_2$ commensurate heterobilayers. *Nat. Commun.* **9**, 1356 (2018).
63. Bellus, M. Z., Ceballos, F., Chiu, H.-Y. & Zhao, H. Tightly bound trions in transition metal dichalcogenide heterostructures. *ACS Nano* **9**, 6459–6464 (2015).
64. Jiang, C. et al. Microsecond dark-exciton valley polarization memory in two-dimensional heterostructures. *Nat. Commun.* **9**, 753 (2018).
65. Zhu, X. et al. Charge transfer excitons at van der Waals interfaces. *J. Am. Chem. Soc.* **137**, 8313–8320 (2015).
66. Nagler, P. et al. Giant magnetic splitting inducing near-unity valley polarization in van der Waals heterostructures. *Nat. Commun.* **8**, 1551 (2017).
67. Kim, J. et al. Observation of ultralong valley lifetime in WSe_2/MoS_2 heterostructures. *Sci. Adv.* **3**, e1700518 (2017).
68. Rivera, P. et al. Valley-polarized exciton dynamics in a 2D semiconductor heterostructure. *Science* **351**, 688–691 (2016).
69. Naik, M. H. & Jain, M. Ultraflatbands and shear solitons in moiré patterns of twisted bilayer transition metal dichalcogenides. *Phys. Rev. Lett.* **121**, 266401 (2018).
70. Yu, H., Wang, Y., Tong, Q., Xu, X. & Yao, W. Anomalous light cones and valley optical selection rules of interlayer excitons in twisted heterobilayers. *Phys. Rev. Lett.* **115**, 187002 (2015).
71. Guo, H., Zhang, X. & Lu, G. Shedding light on moiré excitons: a first-principles perspective. *Sci. Adv.* **6**, eabc5638 (2020).
72. Torun, E., Miranda, H. P. C., Molina-Sánchez, A. & Wirtz, L. Interlayer and intralayer excitons in MoS_2/WS_2 and $MoSe_2$/WSe_2 heterobilayers. *Phys. Rev. B* **97**, 245427 (2018).
73. Zhang, L. et al. Highly valley-polarized singlet and triplet interlayer excitons in van der Waals heterostructure. *Phys. Rev. B* **100**, 041402(R) (2019).
74. Yu, H., Liu, G.-B. & Yao, W. Brightened spin-triplet interlayer excitons and optical selection rules in van der Waals heterobilayers. *2D Mater.* **5**, 035021 (2018).
75. Seyler, K. L. et al. Signatures of moiré-trapped valley excitons in $MoSe_2$/WSe_2 heterobilayers. *Nature* **567**, 66–70 (2019).
76. Rohlfing, M. & Louie, S. G. Electron–hole excitations in semiconductors and insulators. *Phys. Rev. Lett.* **81**, 2312–2315 (1998).
77. Pan, Y. et al. Quantum-confined electronic states arising from the moiré pattern of MoS_2–WSe_2 heterobilayers. *Nano Lett.* **18**, 1849–1855 (2018).
78. Waters, D. et al. Flat bands and mechanical deformation effects in the moiré superlattice of MoS_2-WSe_2 heterobilayers. *ACS Nano* **14**, 7564–7573 (2020).
79. Wu, F., Lovorn, T., Tutuc, E. & MacDonald, A. H. Hubbard model physics in transition metal dichalcogenide moiré bands. *Phys. Rev. Lett.* **121**, 026402 (2018).
80. Zhang, Z. et al. Flat bands in twisted bilayer transition metal dichalcogenides. *Nat. Phys.* **16**, 1093–1096 (2020).
81. Li, E. et al. Lattice reconstruction induced multiple ultra-flat bands in twisted bilayer WSe_2. *Nat. Commun.* **12**, 5601 (2021).
82. Tran, K. et al. Evidence for moiré excitons in van der Waals heterostructures. *Nature* **567**, 71–75 (2019).
83. Jin, C. et al. Observation of moiré excitons in WSe_2/WS_2 heterostructure superlattices. *Nature* **567**, 76–80 (2019).
84. Zhang, N. et al. Moiré intralayer excitons in a $MoSe_2$/MoS_2 heterostructure. *Nano Lett.* **18**, 7651–7657 (2018).
85. Bayer, M., Stern, O., Hawrylak, P., Fafard, S. & Forchel, A. Hidden symmetries in the energy levels of excitonic 'artificial atoms'. *Nature* **405**, 923–926 (2000).
86. Baek, H. et al. Highly energy-tunable quantum light from moiré-trapped excitons. *Sci. Adv.* **6**, eaba8526 (2020).
87. Kremser, M. et al. Discrete interactions between a few interlayer excitons trapped at a $MoSe_2$–WSe_2 heterointerface. *npj 2D Mater. Appl.* **4**, 8 (2020).
88. Bai, Y. et al. Excitons in strain-induced one-dimensional moiré potentials at transition metal dichalcogenide heterojunctions. *Nat. Mater.* **19**, 1068–1073 (2020).
89. Calman, E. V. et al. Indirect excitons and trions in $MoSe_2$/WSe_2 van der Waals heterostructures. *Nano Lett.* **20**, 1869–1875 (2020).
90. Wang, T. et al. Giant valley-Zeeman splitting from spin-singlet and spin-triplet interlayer excitons in WSe_2/$MoSe_2$ heterostructure. *Nano Lett.* **20**, 694–700 (2020).

91. Förg, M. et al. Moiré excitons in $MoSe_2$-WSe_2 heterobilayers and heterotrilayers. *Nat. Commun.* **12**, 1656 (2021).
92. Shinokita, K., Miyauchi, Y., Watanabe, K., Taniguchi, T. & Matsuda, K. Moiré exciton dynamics and moiré exciton-phonon interaction in a WSe_2/$MoSe_2$ heterobilayer. Preprint at https://arxiv.org/abs/2012.08720 (2020)
93. Gammon, D., Snow, E. S., Shanabrook, B. V., Katzer, D. S. & Park, D. Fine structure splitting in the optical spectra of single GaAs quantum dots. *Phys. Rev. Lett.* **76**, 3005–3008 (1996).
94. Toth, M. & Aharonovich, I. Single photon sources in atomically thin materials. *Annu. Rev. Phys. Chem.* **70**, 123–142 (2019).
95. Ren, S., Tan, Q. & Zhang, J. Review on the quantum emitters in two-dimensional materials. *J. Semicond.* **40**, 071903 (2019).
96. Jauregui, L. A. et al. Electrical control of interlayer exciton dynamics in atomically thin heterostructures. *Science* **366**, 870–875 (2019).
97. Choi, J. et al. Twist angle-dependent interlayer exciton lifetimes in van der Waals heterostructures. *Phys. Rev. Lett.* **126**, 047401 (2021).
98. Deilmann, T., Rohlfing, M. & Wurstbauer, U. Light–matter interaction in van der Waals hetero-structures. *J. Condens. Matter Phys.* **32**, 333002 (2020).
99. Madéo, J. et al. Directly visualizing the momentum-forbidden dark excitons and their dynamics in atomically thin semiconductors. *Science* **370**, 1199–1204 (2020).
100. Wallauer, R. et al. Momentum-resolved observation of exciton formation dynamics in monolayer WS_2. *Nano Lett.* **21**, 5867–5873 (2021).
101. Man, M. K. L. et al. Experimental measurement of the intrinsic excitonic wave function. *Sci. Adv.* **7**, eabg0192 (2021).
102. Unuchek, D. et al. Room-temperature electrical control of exciton flux in a van der Waals heterostructure. *Nature* **560**, 340–344 (2018).
103. Unuchek, D. et al. Valley-polarized exciton currents in a van der Waals heterostructure. *Nat. Nanotechnol.* **14**, 1104–1109 (2019).
104. Brem, S., Linderälv, C., Erhart, P. & Malic, E. Tunable phases of moiré excitons in van der Waals heterostructures. *Nano Lett.* **20**, 8534–8540 (2020).
105. Choi, J. et al. Moiré potential impedes interlayer exciton diffusion in van der Waals heterostructures. *Sci. Adv.* **6**, eaba8866 (2020).
106. Yuan, L. et al. Twist-angle-dependent interlayer exciton diffusion in WS_2–WSe_2 heterobilayers. *Nat. Mater.* **19**, 617–623 (2020).
107. Zhang, Y., Yuan, N. F. Q. & Fu, L. Moiré quantum chemistry: charge transfer in transition metal dichalcogenide superlattices. *Phys. Rev. B* **102**, 201115 (2020).
108. Kumar, A., Xie, M. & MacDonald, A. H. Lattice collective modes from a continuum model of magic-angle twisted bilayer graphene. *Phys. Rev. B* **104**, 035119 (2021).
109. Kennes, D. M. et al. Moiré heterostructures as a condensed-matter quantum simulator. *Nat. Phys.* **17**, 155–163 (2021).
110. Andrei, E. Y. et al. The marvels of moiré materials. *Nat. Rev. Mater.* **6**, 201–206 (2021).
111. Regan, E. C. et al. Mott and generalized Wigner crystal states in WSe_2/WS_2 moiré superlattices. *Nature* **579**, 359–363 (2020).
112. Zhou, Y. et al. Bilayer Wigner crystals in a transition metal dichalcogenide heterostructure. *Nature* **595**, 48–52 (2021).
113. Smoleński, T. et al. Signatures of Wigner crystal of electrons in a monolayer semiconductor. *Nature* **595**, 53–57 (2021).
114. Xu, Y. et al. Creation of moiré bands in a monolayer semiconductor by spatially periodic dielectric screening. *Nat. Mater.* **20**, 645–649 (2021).
115. Raja, A. et al. Dielectric disorder in two-dimensional materials. *Nat. Nanotechnol.* **14**, 832–837 (2019).
116. Hsu, W.-T. et al. Dielectric impact on exciton binding energy and quasiparticle bandgap in monolayer WS_2 and WSe_2. *2D Mater.* **6**, 025028 (2019).
117. Li, T. et al. Charge-order-enhanced capacitance in semiconductor moiré superlattices. *Nat. Nanotechnol.* **16**, 1068–1072 (2021).
118. Liu, E. et al. Excitonic and valley-polarization signatures of fractional correlated electronic phases in a WSe_2/WS_2 moiré superlattice. *Phys. Rev. Lett.* **127**, 037402 (2021).
119. Woggon, U. *Optical Properties of Semiconductor Quantum Dots* Vol. 136 (Springer, 1997)
120. Peyghambarian, N., Koch, S. W. & Mysyrowicz, A. *Introduction to Semiconductor Optics* (Prentice Hall, 1993)
121. Haug, H. & Koch, S. W. *Quantum Theory of the Optical and Electronic Properties of Semiconductors* 5th edn (World Scientific, 2009)
122. Gadelha, A. C. et al. Localization of lattice dynamics in low-angle twisted bilayer graphene. *Nature* **590**, 405–409 (2021).
123. McGilly, L. J. et al. Visualization of moiré superlattices. *Nat. Nanotechnol.* **15**, 580–584 (2020).
124. Yoo, H. et al. Atomic and electronic reconstruction at the van der Waals interface in twisted bilayer graphene. *Nat. Mater.* **18**, 448–453 (2019).
125. Li, H. et al. Imaging generalized Wigner crystal states in a WSe_2/WS_2 moiré superlattice. Preprint at https://arxiv.org/abs/2106.10599 (2021)
126. Halbertal, D. et al. Moiré metrology of energy landscapes in van der Waals heterostructures. *Nat. Commun.* **12**, 242 (2021).
127. Padhi, B., Chitra, R. & Phillips, P. W. Generalized Wigner crystallization in moiré materials. *Phys. Rev. B* **103**, 125146 (2021).
128. Zhang, Y., Liu, T. & Fu, L. Electronic structures, charge transfer, and charge order in twisted transition metal dichalcogenide bilayers. *Phys. Rev. B* **103**, 155142 (2021).
129. Morales-Durán, N., MacDonald, A. H. & Potasz, P. Metal-insulator transition in transition metal dichalcogenide heterobilayer moiré superlattices. *Phys. Rev. B* **103**, L241110 (2021).
130. Pan, H. & Das Sarma, S. Interaction-driven filling-induced metal-insulator transitions in 2D moiré lattices. *Phys. Rev. Lett.* **127**, 096802 (2021).
131. Zeng, Y. & MacDonald, A. H. Electrically controlled two-dimensional electron-hole fluids. *Phys. Rev. B* **102**, 085154 (2020).
132. Pan, H., Wu, F. & Das Sarma, S. Quantum phase diagram of a Moiré-Hubbard model. *Phys. Rev. B* **102**, 201104 (2020).
133. Lian, B., Liu, Z., Zhang, Y. & Wang, J. Flat Chern band from twisted bilayer $MnBi_2Te_4$. *Phys. Rev. Lett.* **124**, 126402 (2020).
134. Enaldiev, V. V., Ferreira, F., Magorrian, S. J. & Fal'Ko, V. I. Piezoelectric networks and ferroelectric domains in twistronic superlattices in WS_2/MoS_2 and WSe_2/$MoSe_2$ bilayers. *2D Mater.* **8**, 025030 (2021).
135. Yasuda, K., Wang, X., Watanabe, K., Taniguchi, T. & Jarillo-Herrero, P. Stacking-engineered ferroelectricity in bilayer boron nitride. *Science* **372**, 1458–1462 (2021).
136. Xiao, F., Chen, K. & Tong, Q. Magnetization textures in twisted bilayer CrX_3 (X = Br, I). *Phys. Rev. Res.* **3**, 013027 (2021).
137. Tong, Q., Chen, M., Xiao, F., Yu, H. & Yao, W. Interferences of electrostatic moiré potentials and bichromatic superlattices of electrons and excitons in transition metal dichalcogenides. *2D Mater.* **8**, 025007 (2020).
138. Anđelković, M., Milovanović, S. P., Covaci, L. & Peeters, F. M. Double moiré with a twist: supermoiré in encapsulated graphene. *Nano Lett.* **20**, 979–988 (2020).
139. Wu, F., Lovorn, T. & MacDonald, A. H. Topological exciton bands in moiré heterojunctions. *Phys. Rev. Lett.* **118**, 147401 (2017).
140. Jin, C. et al. Identification of spin, valley and moiré quasi-angular momentum of interlayer excitons. *Nat. Phys.* **15**, 1140–1144 (2019).

Acknowledgements

D.H. and X.L. gratefully acknowledge financial support from the Department of Energy, Basic Energy Science program via grant DE-SC0019398. C.-K.S. and X.L. are partially supported by NSF MRSEC under Cooperative Agreement No. DMR-1720595. J.C. and X.L. acknowledge financial support from NSF DMR-1808042 and the Welch Foundation F-1662. C.-K.S. acknowledges financial support from the Welch Foundation via F-1672.

Competing interests

The authors declare no competing interests.

Additional information

Correspondence should be addressed to Di Huang or Xiaoqin Li.

Peer review information *Nature Nanotechnology* thanks the anonymous reviewers for their contribution to the peer review of this work.